Direct Observations of Magnetic Reconnection Sites of An Eruption on November 18, 2003

J. Lin[1], Y.-K. Ko[1], L. Sui[2], J. C. Raymond[1], G. A. Stenborg[2], Y. Jiang[3], S. Zhao[3], and S. Mancuso[1,4]

ABSTRACT

This work reports direct observations of the magnetic reconnection site during an eruptive process occurring on November 18, 2003. The event started with a rapid expansion of a few magnetic arcades located over the east limb of the Sun and developed an energetic partial halo coronal mass ejection (CME), a long current sheet and a group of bright flare loops in the wake of the CME. It was observed by several instruments both in space and on ground, including the EUV Imaging Telescope, the Ultraviolet Coronagraph Spectrometer, and the Large Angle and Spectrometric Coronagraph experiment on board the *Solar and Heliospheric Observatory*, the Reuven Ramaty High Energy Solar Spectroscopic Imager, as well as the Mauna Loa Solar Observatory Mark IV K-coronameter. We combine the data from these instruments to investigate various properties of the eruptive process, including those around the current sheet. The maximum velocities of the CME leading edge and the core were 1939 km s^{-1} and 1484 km s^{-1}, respectively. The average reconnection inflow velocities near the current sheet over different time intervals ranged from 10.5 km s^{-1} to 106 km s^{-1}, and the average outflow velocities from 460 km s^{-1} to 1075 km s^{-1}. This leads the corresponding rate of reconnection in terms of the Alfvén Mach number M_A to ranging from 0.01 to 0.23. The composite of images from different instruments specifies explicitly how the different objects developed by a single eruptive process are related to one another.

[1]Harvard-Smithsonian Center for Astrophysics, 60 Garden Street, Cambridge, MA 02138, USA.

[2]Department of Physics, Catholic University of America, 620 Michigan Avenue, Washington, DC 20064, USA.

[3]National Astronomical Observatories of China/Yunnan Observatory, Chinese Academy of Sciences, P. O. Box 110, Kunming, Yunnan 650011, China

[4]INAF/Osservatorio Astronomico di Torino, 20 Strada Osservatorio, I-10025 Pino Torinese, Italy.

Subject headings: Sun: eruptions − Sun: flares − Sun: coronal mass ejections − Magnetic reconnection

1. Introduction

The catastrophe model of solar eruptions suggests that the major eruptive processes occurring in the solar atmosphere be triggered by the catastrophic loss of mechanical equilibrium in the magnetic configuration (e.g., Forbes 2000; Priest & Forbes 2002; Lin et al. 2003). As the catastrophe takes place, the closed magnetic field lines in the configuration are stretched so severely that they effectively open up, and a current sheet forms separating two magnetic fields of opposite polarities. With the dissipation occurring in the current sheet, the stretched field lines reconnect and create new closed field lines below the current sheet (see Figure 1). Generally, the time scale of magnetic dissipation or reconnection is long compared to that of the catastrophe, which is the Alfvén time scale, so the development of a long current sheet during the major eruptions is expected (Lin & Forbes 2000; Forbes & Lin 2000).

As indicated by Figure 1, the current sheet is dissipated by magnetic reconnection, so that the catastrophe is able to develop to a plausible eruption. Subsequently, reconnection dumps a large amount of energy in the lower atmosphere of the Sun, which accounts for the traditional flare ribbons and loops; meanwhile, magnetic reconnection also sends large amount of the reconnected flux and plasma upward, accounting for the rapid expansion of the ejecta and the hot shell surrounding the ejecta (e.g., Lin et al. 2004).

As a result of the high electrical conductivity and the force-free environment in the corona, the current sheet is confined to a very local and thin region. This makes direct observation of the current sheet extremely difficult (refer to Ko et al. 2003 for the discussions and brief review on this issue). Therefore, information about magnetic reconnection inside the current sheet is usually deduced indirectly by observing the dynamic behaviors of the products of magnetic reconnection, such as the separating flare ribbons on the solar surface (Poletto & Kopp 1986; Qiu et al. 2002; Wang et al. 2003; Qiu et al. 2004), the growing flare loops in the corona (Sui & Holman 2003; Sui et al. 2004), and so on. The magnetic reconnection inflow around the X-type neutral point over the flare loops was also reported and used to analyze the properties of magnetic reconnection in an eruptive process (Yokoyama et al. 2001).

Utilizing the ultraviolet spectroscopic observations from the Ultraviolet Coronagraphic Spectrometer (UVCS) on board the *Solar and Heliospheric Observatory (SOHO)*, together

with other remote-sensing data, Ciaravella et al. (2002) and Ko et al. (2003) conducted comprehensive analyses from various aspects on several eruptive processes that clearly manifested both coronal mass ejections (CMEs) and solar flares, and confirmed the existence and development of the long current sheet in the events as predicted by Lin & Forbes (2000). Webb et al. (2003) surveyed 59 CMEs observed by the Solar Maximum Mission from 1984 to 1989, and found that about half were followed by co-axial, bright rays suggestive of newly formed current sheets. They concluded that the characteristics of these structures were consistent with the Lin and Forbes model.

The event of November 18, 2003 provides us another opportunity to observe directly the presumed current sheet and the associated magnetic reconnection process. It was observed by instruments both in space and on the ground. We display the observational data and give the corresponding results in the next section, and then discuss and summarize the present work in Section 3.

2. Observations and Results

This event occurred on the east limb of the Sun. No apparent magnetic structure appeared in the region nearby in Hα filtergrams. After having looked at both the magnetograms obtained by the Michelson Doppler Imager (MDI) on board the *SOHO* and the Hα images obtained on ground within the following three successive days, we find that the eruption took place between the two active regions, AR0507 and AR0508, located north and south of it, respectively, but its relations to these two active regions are not clear. On the other hand, the initial stage and the subsequent development of the eruption in the lower corona were clearly recorded in 195 Å by the EUV Imaging Telescope (EIT) on *SOHO*, and the Reuven Ramaty High Energy Solar Spectroscopic Imager (RHESSI, Lin et al. 2002). The consequences in the higher corona were observed by UVCS and the Large Angle and Spectrometric Coronagraph Experiment (LASCO) on *SOHO*, and the Mauna Loa Solar Observatory Mark IV K-coronameter (MLSO MK4).

We were first impressed by this event that the magnetic structures were severely stretched by the eruption, and that the two legs of the stretched structures soon started moving toward one another approaching the presumed current sheet located between them. We were then impressed with morphological features of the CME developed during the eruption. Figure 2 displays a set of snapshots of the eruption at the initial phase observed in 195 Å by EIT. The corresponding movies are available at both http://hesperia.gsfc.nasa.gov/~ sui/20031118/eruption.gif and http://hesperia.gsfc.nasa.gov/~sui/20031118/eit_loop.gif. The former displays the apparent motions of the stretched magnetic structures near the presumed

current sheet and the growing of the cusp point, and the latter emphasizes the associated flare loops. Figure 3 shows the magnetic structures before and after the CME passed through the field of views of LASCO C2 and C3. The snapshots in Figure 4 give more details of the CME and the subsequent evolutionary features observed by C2 (see also the movie that is available at http://hesperia.gsfc.nasa.gov/~sui/20031118/C2_031118_wavelet.mpg), and Figure 5 specifies a composite of C2, UVCS and EIT 195 Å images, which manifests clearly the objects at various altitudes developed by a major eruptive process. These objects show the similarity between the observations of a CME-current sheet and the model shown by Figure 1.

The LASCO C2 images shown in Figures 4 and 5 have been enhanced by the wavelet technique of which more details will be provided and discussed shortly. We arrange these figures this way to provide the reader with the entire sequence of the eruption, as well as the key characteristics that we are focusing on in the present work. The relevant data, the tools we are using to process these data, and our detailed analyses and investigations are explained next.

2.1. Observations in EIT 195 Å, in RHESSI Soft X-Rays, and in MK4 White-Light

The EIT 195 Å images taken in the time interval of interest have a field of view of 1.4 $R_\odot \times 1.4\, R_\odot$ and a resolution of $5.3''$/pixel. Before the eruption took place, a group of bright arcades in EIT 195 Å distributed at both sides of the equator could be seen clearly. The EIT 195 Å movie shows that the central arcade started to change at around 08:48 UT. A small, faint arcade-like structure became distinguishable from the background (Figure 2a). As it expanded outward, it split into three small arcades with the middle one being the brightest (Figure 2b). The outer arcade exploded between 9:00 UT and 9:12 UT, and the middle one followed between 9:12 UT and 9:24 UT. The horizontal arrows in the relevant panels indicate these arcades, and the red arrow indicates the direction of expansion. Associated with the explosion of the middle arcade, two legs of the arcade system were quickly stretched out and separated from one another, with the northern one moving much faster than the southern one (Figure 2c. Note the red arrow). (The reasons that the two legs behave differently will be discussed shortly.) Then, these two legs began to approach one another from 9:36 UT (Figure 2d. Note the red arrows in this panel and in the following ones), which implies an inflow motion of magnetic reconnection driven by the eruption. Subsequently, a sharp bright cusp structure formed and moved upwards continuously (Figures 2f through 2h. Note the white arrows). This process is quite similar to that in an eruption reported by Yokoyama et

al. (2001), which also showed apparent reconnection inflow near the cusp point.

Following Yokoyama et al. (2001), we can measure the velocity at which the legs of the extended arcades approach to one another, and use it as the velocity of the magnetic reconnection inflow near the reconnection site (e.g, the X-type neutral point or the current sheet). However, the structure seen in EIT images is diffuse, and an accurate speed is difficult to determine. Moreover, Chen et al. (2004) re-analyzed the observations of Yokoyama et al.. They suggest that that the apparent inward motion was actually due to a changing position of the X-type reconnection region rather than inflow. Therefore, we will use the UVCS observations (see Section 2.3), rather than EIT images, to determine the inflow speed.

From 11:24 UT, the top of the cusp structure started to become round, and its height also decreased (Figures 2j and 2k), manifesting an apparent shrinkage process (see Švestka et al. 1987; Lin et al. 1995; and Forbes & Acton 1996). Then, the cusp structure disappeared from the EIT field of view. Instead, a group of bright flare loops appeared at successively higher altitudes (Figures 2k through 2o). The growth of flare loops observed in EIT 195 Å lasted more than 20 hours, and the flare loops were still visible in the following days. The red arrows in Figures 2k, 2l, and 2m point to another flare loop system that started to form at around 11:48 UT. We will discuss it later.

According to the standard theory of two-ribbon flares (e.g, Forbes & Acton 1996, and the references therein), some fine structures of magnetic field and plasma should exist between the cusp point and the post-flare loops (Figure 1). These features include a Mach 2 jet, a termination shock, condensation inflow, shock enhanced cooling, and so on (see the details shown in the lower panel in Figure 1). (We note that the Mach 2 jet is actually the reconnection outflow from the current sheet located above the cusp point, and that the Mach number here is the outflow speed compared to the Alfvén speed in the outflow region, instead of that in the inflow region as we use at most places in the present work.) Usually these features would not be distinguishable either due to the lower resolution of the images or due to the scattered light from the objects nearby. To look into these features, we apply the technique of wavelet-based intensity contrast-enhancement (WICE) to process those images in Figure 2. Detailed descriptions and discussions about this technique can be found in the works by Starck et al. (1997) and by Stenborg & Cobelli (2003). The advantage of the images obtained this way is that the small scale features of magnetic field embedded within large scale structures can be enhanced significantly.

The enhanced EIT images do not show significant differences at large scales from those in Figure 2, but the flare loops below the cusp region began to be visible from 10:24 UT (see the left panel in Figure 6) when the cusp structure is still visible in EIT 195 Å images. The apex of the loop system is not just right beneath the cusp point. Instead they were separated

by a distance of around 6.5×10^4 km. This distance was not constant, but increased with time (see the other 3 panels in Figure 6). In the panels taken at 10:24 UT, 10:36 UT and 11:00 UT, we also notice a short and bright stem-like feature between the cusp point and the top of flare loops. This feature exists for about an hour from 10:14 UT to 11:12 UT, and is brightest within the time interval between 10:24 UT and 11:00 UT. Furthermore, a faint loop-like gap exists between the lower tip of this feature and the top of the bright EIT 195 Å loops (see the left two panels in Figure 6). Comparing the details shown by Figure 1, we find that this feature is just located where the Mach 2 reconnection jet and the termination shock should appear, and that the faint loop-like gap seen in the enhanced EIT 195 Å images or movies is probably the position where the hot ($\sim 10^7$K) soft X-ray loops, together with the shock enhanced cooling, should sit according to the standard model for two-ribbon flares (see also Forbes & Malherbe 1986; and Forbes & Acton 1996). More dynamical details of the above process can be seen clearly from the movies (animations) that we mentioned above.

In addition to the observations in EIT 195 Å, the above cusp structure was also observed by RHESSI. The tip of the cusp in the RHESSI images was about 7×10^4 km above the limb (Figure 7). The two RHESSI images used in this work were obtained within the time interval from 09:37 UT to 10:23 UT. The early rising phase of the event was missed due to the South Atlantic Anomaly and the Earth eclipse (RHESSI's night time). The soft X-ray (< 25 keV) peaked around 10:00 UT. No apparent hard X-ray emission (energy > 25 keV) was observed. But the RHESSI images at energies below 25 keV show clearly a loop-like structure, and those in the channel from 12 keV to 16 keV observed between 09:39 and 10:05 UT obviously displayed a cusp structure on the top of the flare loops. Two such images are overlaid on an EIT 195 Å image in Figure 7. The field of view of these two images is about $200'' \times 200''$. The cusp feature observed in X-ray emissions clearly coincides in space with that in EIT 195 Å.

After the cusp structure disappeared from the EIT field of view, it still could be seen at higher altitude as shown in the MLSO MK4 white-light images. Figure 8 is a composite of LASCO C2 (at 17:50 UT), MK4 (at 17:49 UT) and EIT 195 Å (at 17:48 UT) images, which clearly manifests the positions of the post-flare/CME loops, cusp point and the extended current sheet. Obviously, Figure 8 resembles the typical Kopp-Pneuman configuration of major flares (see Kopp & Pneuman 1976; Forbes & Acton 1996; and the references therein), in which the post-flare/CME loops are located under the cusp structure at the lower tip of the current sheet, and the upper tip of the current sheet extends to a large distance.

2.2. Observations by LASCO C2 and C3

Prior to the event, a helmet streamer was present at position angle (PA) about 135° (Figure 3a) measured from the Solar North counter-clockwise. Comparison with the Hα and MDI images suggests that it was located over either AR0506 or AR0508. Following the explosion observed in EIT 195 Å, the front of a fast CME appeared in the field of view of LASCO C2 at 9:26 UT and in that of LASCO C3 at 10:42 UT, showing the typical three-component structure of CMEs with a big bright core (Figures 3b). According to the SOHO/LASCO CME Catalog, it is a partial halo CME with angular width > 197°. The motion of the CME core remains in the plane of PA = 96°, which is very close to the equatorial plane.

2.2.1. CME in LASCO Field of View

Comparing Figure 3a with Figure 8 indicates that the helmet streamer was located very close to the region where the eruption took place. Interaction between the magnetic field involved in the eruption and that of the helmet streamer may be expected. With the data we are able to collect, we lack direct evidence of the interaction. However, such interaction can be conjectured from the following observational facts: The existence of the helmet streamer tends to prevent the eruptive arcades from moving southward (note the red arrow in Figure 2c), which suggests that the magnetic fields in both structures have the same orientation but belong to two different magnetic systems without topological connections. Interaction with the helmet streamer also tends to push the CME to propagate northward. With the magnetic field in the helmet streamer getting weaker at higher altitudes and with rapid expansion of the CME bubble, however, the helmet streamer was deflected toward the south (Figures 3b). The deflection was so severe that the magnetic fields of opposite orientations in the helmet streamer were driven to reconnect with one another. The EIT 195 Å movie indicates that the reconnection occurred at around 12:24 UT with the newly formed flare loops located south to those developing earlier as the signature. Readers themselves may look at the movie which is available on the *SOHO* website, or compare the details of the bright features indicated by the red arrows in Figures 2l and 2m. Subsequently, the southern leg of the CME (disrupting arcade) merged with the northern leg of the helmet streamer and formed a new helmet streamer (Figures 3c and 3d), which looked like the old one. This case is different from those in which CMEs blow away the helmet streamer from inside (e.g, Raymond et al. 2003 and the references therein).

Meanwhile, the interaction caused the evolution of morphological structures of the CME to be very non-uniform as well. Figure 9 displays the height-time profiles of three different

positions of the CME, as well as the deduced velocities and accelerations. The panels in Figure 9a shows the results for the CME core measured at PA = 96°. The top panel plots the height versus time. The solid points give the observed data and the curve shows the fitting result based on the following formula:

$$h(t) = a_1 + a_2 t + a_3 t^2 e^{-a_4 t}, \tag{1}$$

where a_1 through a_4 are the fitting co-efficients, h is the height in units of km, t is the time in seconds, and we set 09:00 UT as $t = 0$ when doing the curve fitting. The corresponding velocities dh/dt and accelerations d^2h/dt^2 are then deduced from (1), and they are plotted versus time in another two panels in Figure 9a. The second row of Table 1 lists a_1 through a_4, and the maximum velocity v_{max}, as well as the corresponding time t_{max} and height h_{max} for the CME core as measured at PA = 96°. The non-uniform expansion of the CME bubble can be investigated by tracking some points on the CME leading edge. In the present work, we choose two points located at PA = 88° and PA = 100°, respectively, on the leading edge. Two sets of data for height versus time are obtained. We plot these data in the top panels of Figures 9b and 9c, respectively, and fit them to the curve described by (1). The corresponding velocities and accelerations are plotted in another two panels of the above figures. The fitting co-efficients, the maximum velocities together with the corresponding time t_{max} and height h_{max}, deduced from (1) are listed in the third and fourth rows of Table 1.

More details of morphological features of the CME can be further seen from the enhanced C2 images. Figure 4 displays a set of such images that have been processed by the WICE technique. These images cover the time interval from 09:50 UT to 21:26 UT. The fine structures that need to be highlighted include the leading edge and the core of CME (see the images of 10:06 UT and 10:26 UT), the characteristics of magnetic field around the current sheet (see the images of 10:50 UT and 11:26 UT), and the current sheet itself (see the images of 12:50 UT, 14:26 UT, 16:26 UT, and 21:26 UT). From this set of images, one may also see clearly the helmet streamer at PA 135° being deflected from outside by the CME through comparing the image of 09:50 UT with others. The helical structure around the CME core is also worth noticing (images of 10:06 UT and 10:26 UT in Figure 4). It shows apparently a shape of the flux rope surrounded by a bubble (e.g., Lin et al. 2004). Readers may find more information by watching the corresponding movie (animation) that has been mentioned in Section 2.

2.2.2. Reconnection Outflow along Current Sheet

Following the tangled structure of the CME, a long and thin streamer-like feature appeared in the field of view of LASCO C2 and then C3, and several bright blobs successively flowed away from the Sun along this feature (see Figures 3c and 3d). This thin streamer-like structure initially appeared at PA = 90° and moved slowly toward the south approaching PA = 116°, which suggests a process of the self-adjustment of the disrupted magnetic field as the eruption was in progress. During this process, several blobs were recognized and we investigated the motions of five of them with good resolution. The heights of these five blobs are plotted versus time in Figure 10, and the curves are used to fit the data on the basis of the following quadratic relation:

$$h(t) = b_1 + b_2 t + b_3 t^2, \tag{2}$$

where h is in units of km, t is in seconds, and the time shown at the left-lower end of each panel in Figure 10 is set as $t = 0$ for the corresponding blob. The values of these coefficients are listed in Table 2 for each of the five blobs. The motion of blob one manifested apparent acceleration of 158 m s^{-2}, that of blob two showed deceleration of 42.5 m s^{-2}, and another three blobs moved with slight acceleration varying from 16.7 m s^{-2} to 26.7 m s^{-2}. We also calculated the average velocities for all five blobs, which are listed in column 6 of Table 2. It is interesting that the motion of blob one showed the largest acceleration, but its average speed was the lowest one (460 km s^{-1}); on the other hand, blob two moved with deceleration and its average speed was the highest one (1075 km s^{-1}). From the time shown in Figure 10, we also notice that magnetic reconnection associated with this event was still in progress after 21:00 UT of November 19, 2003. This implies that the whole process of the event lasted for more than 36 hours, which is the typical behavior of a long duration event.

After comparing the above process and characteristics displayed by the thin streamer-like structure shown in Figures 3 and 8 with those displayed by the current sheet developing in another event investigated by Ko et al. (2003), we believe that this thin structure in the present case is also the current sheet developing in the wake of the CME, and those blobs depicted the outflow due to magnetic reconnection inside the current sheet. The change in the velocities of those blobs suggests that the current sheet was not uniform, and that the rate of magnetic reconnection varied with time and position.

2.3. Observations by UVCS

During the above observations, the UVCS experiment also observed this CME event during one of its synoptic scans. At 10:04 UT the UVCS slit was placed at 1.70 $R_\odot$ at PA =

90° and five 120-second exposures were acquired (see the left UVCS image in Figure 5). The corresponding distributions of Lyα intensities along the slit are given in Figure 11a. The slit was then moved to 1.52 $R_\odot$ and four more exposures were taken (see the right UVCS image in Figure 5), and the Lyα intensity distributions are given in Figure 11b.

The data reported here were taken from the O VI channel. The slit width was set to 150 μm which corresponds to an instantaneous field of view of $40' \times 42''$. The synoptic data were obtained with a spatial binning of 3 pixels (21$''$) and a spectral binning of 2 pixels (0.183 Å for Lyα). The raw data have been wavelength and flux calibrated. The uncertainty in the flux calibration is about 20% for the first order lines (Gardner et al. 2000). Stray light is negligible in the data so no stray light correction is performed.

Figure 5 gives a composite of a C2 image at 10:26 UT that has been enhanced by the WICE technique, an EIT image at 10:14 UT, and two images of the UVCS slit located at 1.70 R$_\odot$ and 1.52 R$_\odot$, respectively. The UVCS image at left is created by stacking 5 exposures of the Lyα intensity distributions along the UVCS slit taken at 1.70 R$_\odot$, which covers the time interval from 10:04 UT to 10:14 UT; and that at right is created by stacking 4 exposures of the Lyα intensity distributions along the UVCS slit taken at 1.52 R$_\odot$, which covers the time interval from 10:17 UT to 10:23 UT. So, the horizontal scale of the UVCS images does not represent the extension in space, but in time. Comparing with those at the corresponding times shown in Figure 2, one can easily find that the dark gap in UVCS image at early times coincided with the separating motions of two legs of the eruptive arcades in both space and time, and that this gap gradually disappeared as a result of the reconnection inflow near the current sheet. The process in which the gap disappeared can also be seen from the changes in the profiles of Lyα intensities shown in Figure 11a. Its importance for the velocity diagnostic will be investigated below.

During the 4 exposures at 1.52 R$_\odot$, the gap was barely visible, but a bright feature was apparent at a position angle of PA = 88° (see the right UVCS image in Figure 5 and the curves in Figure 11b). This feature brightened rapidly, from 3.8×10^{11} erg cm^{-2} s^{-1} sr^{-1} between 10:16 UT and 10:18 UT to 1.4×10^{12} erg cm^{-2} s^{-1} sr^{-1} between 10:20:26 UT and 10:22:34 UT in Lyα. It was visible in low temperature lines: H I Lyman lines, C III λ977, N III λ991, O VI $\lambda\lambda$ 1023, 1037 and Si III λ1206.5. The bright feature was about 10 times as bright as neighboring regions in Lyα, but only about twice as bright in O VI. We do not have a reliable density diagnostic in this case, but the brightening can easily be accounted for by lower temperature plasma spanning the range 7×10^4 to 3×10^5 K with a density similar to that in adjacent regions along the slit. We interpret the low temperature feature as material in one of the CME legs that are often visible in UVCS observations as sharp features seen in cool lines for a long time (Ciaravella et al. 2000).

2.3.1. Velocity Diagnostic

The above dimming and recovery process observed in Lyα by UVCS is also important for the diagnostic of the magnetic reconnection inflow velocities near the current sheet. The spatial distributions of the Lyα intensities along the UVCS slit shown in (Figure 11a) manifest an apparent low emission area. This area corresponds to the dark gap seen in the UVCS image at left in Figure 5 and existed at around PA 95° indicating coronal dimming as a result of the eruption. The width of this gap decreased with time, indicating the inflow of magnetic reconnection and the coincidence of the current sheet with the gap in space. Comparing the widths of the gap of every two successive times helps deduce the velocities of the reconnection inflow, V_R. Five Lyα intensity profiles yield four values of V_R: 73.2, 106, 36.6, and 10.5 km s^{-1}, respectively. Strictly speaking, they are the average values over four periods: 10:04:15 UT $-$ 10:06:45 UT, 10:06:45 UT $-$ 10:09:13 UT, 10:09:13 UT $-$ 10:11:41 UT, and 10:11:41 UT $-$ 10:14:11 UT (Figure 11a). Comparing these velocities to the local Alfvén speed, V_A, in the reconnection inflow region yields the rate of magnetic reconnection in terms of the inflow Alfvén Mach number, M_A, namely $M_A = V_R/V_A$.

In the present case, we have identified the blobs as the magnetic reconnection outflows along the current sheet. According to the standard theory of magnetic reconnection (e.g., Priest & Forbes 2000), the velocities of the blobs are either equal to V_A if the plasma is incompressible, or differ from V_A by a factor of the square root of the plasma density of the inflow region compared to that of the outflow region. In reality, the plasma is compressible, but the numerical experiments indicate that the above factor varies between 1 and 2 in the coronal environment (e.g., Forbes & Malherbe 1986). So, the incompressible plasma is a good approximation for the process occurring in the corona. This therefore gives the values of M_A in the range from 0.01 to 0.23. In principle, M_A is a function of both space and time, as well as of the parameters for the current sheet, such as the length scale and the resistivity. However, there is no theory that describes rigorously how M_A depends on these parameters, especially when the eruption is in the phase of rapid evolution. Hence, what we can say about our results, for the time being, is that the real value of M_A in the present case should vary over a wider range than that deduced above because our calculations are based on the average values of both V_R and V_A.

2.3.2. Temperature Diagnostic

To further confirm that the dark gap in UVCS images is the region where the current sheet is located, we also look into the properties of other spectral lines. Generally, such a dark gap in UVCS images could correspond to the traditional EIT dimming (Harrison et

al. 2003; Thompson et al. 2000; and references therein), which resulted from the severe stretching of the disrupted magnetic field and the consequent transient depletion of the plasma density. However, because the Lyα intensity depends on the HI neutral fraction and on Doppler dimming, the gap could result from a higher temperature or a significant outflow speed.

Figure 12 shows three Lyα profiles averaged over the 5 exposures at 1.70 R$_\odot$ in the gap and at positions to the north and south. We note that the existence of the gap does not necessarily mean that the emission from this region vanishes, instead it just implies that the emission from this region is lower than that from the regions nearby. In the average profiles, the Lyα width in the gap is considerably larger than in the regions to the north and south, suggesting higher temperature. However, the individual exposures show that the Lyα line width measured at the center of the gap (PA = 93.2° to 96.8°) decreases from 2.24 Å (FWHM) during the first exposure to 1.25, 1.18, 1.12 and 1.06 Å in the subsequent exposures. This can be compared with a line width 1.09 Å south of the gap. If the line width were taken as the thermal width, the temperature in the gap would be 6.7×10^6 K in the first exposure. However, a temperature this high would require a density of above 10^8 cm^{-3} to account for the Lyα intensity, and this would imply an easily detectable signal in the [Fe XVIII] λ974.8 line. Therefore we conclude that the low Lyα intensity is not due to high temperature, but is due either to a smaller density or to Doppler dimming (Noci et al. 1987 and references therein). An outflow speed of 200 km s^{-1} would account for the low intensities in the gap if the densities are similar to those outside of it. The large line width in the first exposure would then be attributed to the line-of-sight component of the outflow. Because we identify the gap with the feature seen as a modest density enhancement in LASCO images at larger heights, we believe that Doppler dimming is the explanation for the low emission.

In principle either the gap seen at 1.70 R$_\odot$ or the cool region seen at 1.52 R$_\odot$ might be associated with the bright ray seen in LASCO about an hour later. Based on the position angle of the LASCO filament of 96°, the position of the gap at 1.70 R$_\odot$ (96°) and the cool plasma at 1.52 R$_\odot$ (87°), the ray seen in white light is associated with the Lyα gap, while the cool material farther north is associated with a fainter, more diffuse material seen in Figure 8 just north of the equator. While it seems counterintuitive to identify a bright feature in white light with a dark feature in Lyα, a substantial outflow speed is common to both.

It is also worth noting that the Lyα profiles to the north and south of the gap are shifted with respect to the centroid of the Lyα profile in the gap by about -20 and +35 km s^{-1}, respectively. This could indicate a line-of-sight component of the same motion seen as the narrowing of the gap. Alternatively, Kopp & Pneuman (1976) predict substantial outflow

along field lines adjoining the current sheet. If those field lines are tilted toward and away from the Earth, Doppler shifts like those observed would naturally occur.

3. Discussion and Conclusions

Following Ciaravella et al. (2002), Ko et al. (2003) and Webb et al. (2003), the current sheet developing in the wake of a CME is investigated once again. The event discussed here occurred on the east limb of the Sun on November 18, 2003. It started from 08:48 UT with the fast expansion of a group of sheared arcades. No apparent prominence structure can be recognized in either Hα filtergrams or EIT 195 Å images prior to the eruption. This event developed a long and thin current sheet behind the CME. The magnetic reconnection inflow near the current sheet following the arcade expansion was observed, and the corresponding rate of magnetic reconnection M_A ranges from 0.01 to 0.23. The value of M_A in reality may not be constant and should cover a wider range.

A similar process of magnetic reconnection inflow was also reported by Yokoyama et al. (2001) for the event on March 18, 1999. But the inflow velocity and M_A deduced by them are both one order of magnitude smaller than what we obtained in the present case. Another difference between two events lies in the initial configurations. The magnetic arcades in the present case possess a much more compact structure than those of Yokoyama et al. (2001). The event observed by Yokoyama et al. (2001) started with the expansion of a feature that clearly manifests the "three-component" structure: a "bright leading edge", a dark "void" or "cavity", and a "bright core". Here, we are quoting the relevant terms because they are traditionally used for CMEs in progress (see Hundhausen et al. 1994 and Low 2001), instead of for the structures prior to the eruption.

One of the advantages of this work over that of Yokoyama et al. (2001) is that the reconnection outflow in the present case might be observed. This allows us to estimate V_A directly in the reconnection inflow region in a more reliable way without making any extra assumptions. Furthermore, the UVCS observations make it possible for us to avoid unnecessary confusion in measuring the inflow speed of reconnection (e.g., see Chen et al. 2004).

The morphological features of the CME developed by this event shown in Figure 5 nearly duplicate those of the cartoon shown in Figure 1, which schematically describes the disrupted magnetic field that forms in the eruptive process following the catastrophic loss of equilibrium in the magnetic system. Comparing Figures 8 with 5 further suggests that the typical Kopp-Pneuman structure is the low-corona component of a disrupting magnetic

field. It is this disrupting magnetic field that gives both the major flare and the CME. Of course, the configuration in Figure 1 can also be produced in the process described by other CME models, such as the sheared arcade and the break-out models (Mikić et al. 1988; Mikić & Linker 1994; Antiochos et al. 1999; Amari et al. 2003; and Linker et al. 2003). Recently, Antiochos (2004) comprehensively compared the disrupted configuration produced by the catastrophe and that by the break-out, and concluded that they should have the same topological structure. The difference lies in the fact that the plasma inside the flux rope (CME core) in the former case should be cool (the prominence material) and that in the latter one is hot (the reconnected plasma flowing out of the current sheet). In the present case, the observations by UVCS just missed the CME core and no information regarding the temperature of the plasma in the core could be drawn. Therefore, analyzing the available data for this event cannot help determine which mechanism triggers the eruption.

The eruptive process manifests an energetic CME with the speeds of the front edge of 1939 km/s and of the CME core of 1484 km/s, respectively, and a bright flare loop system covered by a cusp structure. This event was observed by various instruments from both space and ground. Analyzing the observational data from these instruments yields the conclusion that the CME and the flare are connected by a stretched current sheet in which magnetic reconnection occurs and converts the magnetic energy into the heat and the kinetic energy. The morphological features of the disrupted magnetic field involved in this event fit those of the cartoon shown in Figure 1 very well, which implies that the cartoon depicts the common characteristics of the eruptive processes that give rise to both flare and CME. The magnetic configuration in reality may be much more complex than that shown in the cartoon, but the fundamental physical processes should be the same!

REFERENCES

Amari, T., Luciani, J. F, Aly, J. J., Mikić, Z., and Linker, J. 2003, ApJ, 585, 1073.

Antiochos, S. K. 2004, invited paper presented at Working Group 2 of SHINE 2004.

Antiochos, S. K., DeVore, C. R., and Klimchuk, J. A. 1999, ApJ, 510, 485.

Chen, P. F., Shibata, K., Brooks, D. H., & Isobe, H.: 2004, ApJ, 602, L61.

Ciaravella, A., Raymond, J. C., Li, J., Reiaer, P., Gardner, L. D., Ko, Y.-K., & Fineschi, S. 2002, ApJ, 575, 1116.

Ciaravella, A., Raymond, J. C., Thompson, B. J., van Ballegooijen, A. A., Strachan, L., Li, J., Gardner, L., O'Neal, R., Antonucci, E., Kohl, J., & Noci, G. 2000, ApJ, 529, 575.

Forbes, T. G. 2000, J. Geophys. Res., 105, 23153.

Forbes, T. G., & Acton, L. W. 1996, ApJ, 459, 330.

Forbes, T. G., & Malherbe, J. M. 1986, ApJ, 302, L67.

Gardner L. D., Atkins, N., Fineschi, S., Smith, P. L., Kohl, J. L., Maccari, L., & Romoli, M. 2000, in Instrumentation for UV/EUV Astronomy and Solar Missions, SPIE Proceedings, Vol.4139, (eds.) S. Fineschi, C. M. Korendyke, O. H. Siegmund, & B. E. Woodgate, p. 362.

Harrison, R. A., Bryans, P., Simnett, G. M., and Lyons, M. 2003, A&A, 400, 1071.

Hundhausen, A. J., Stanger, A. L., and Serbicki, S. A. 1994, in Solar Dynamic Phenomena and Solar Wind Consequences (Noordwijk: ESTEC, the Netherlands), p. 409.

Kopp, R. A., & Pneuman G. W. 1976, Sol. Phys., 50, 85.

Ko, Y., Raymond, J. C., Lin, J., Lawrence, G., Li, J., & Fludra, A. 2003, ApJ, 594, 1068.

Lin, J. 2002, Chinese J. Astron. Astrophys., 2, 539.

Lin, J., & Forbes, T. G. 2000, J. Geophys. Res., 105, 2375.

Lin, J., Forbes, T. G., Priest, E. R., & Bungey, T. N. 1995, Sol. Phys., 159, 275

Lin, J., Raymond, J. C., & van Ballegooijen, A. A. 2004, ApJ, 602, 422.

Lin, J., Soon, W., & Baliunas, S. L. 2003, NewA Rev., 47, 53.

Lin, R. P., et al., 2002, Sol. Phys., 210,3.

Linker, J. A., Mikić, Z., Lionello, R., Riley, P., Amari, T., and Odstrcil, D.: 2003, *J. Plasma Phys.*, 10(5), 1971.

Low, B. C. 2001, J. Geophys. Res., 106, 25141.

Mikić, Z., Barnes, D. C., & Schnack, D. D. 1988, ApJ, 328, 830.

Mikić, Z., and Linker, J. A. 1994, ApJ, 430, 898.

Noci, G., Kohl, J. L., & Withbroe, G. L. 1987, ApJ, 315, 706.

Poletto, G., & Kopp, R. A.: 1986, in *The Lower Atmosphere of Solar Flares*, (ed.) D. F. Neidig, NSO, Sunspot, NM, P. 453.

Priest, E. R., & Forbes, T. G.: 2000, *Magnetic Reconnection − MHD Theory and Applications*, Cambridge: Cambridge Univ. Press.

Priest, E. R., & Forbes, T. G. 2002, A&A Rev., 10, 313.

Qiu, J., Lee, J., Gary, D. E., Wang, H.: 2002, ApJ, **565**, 1335.

Qiu, J., Wang, H., Cheng, C. Z., & Gary, D. E.: 2004, ApJ, 604, 900.

Raymond, J. C., Ciaravella, A., Dobrzycka, D., Strachan, L., Ko, Y.-K., Uzzo, M. M., & Raouafi, A.-E. 2003, ApJ, 597, 1106.

Stenborg, G., Cobelli, P. 2003, A&A, 398, 1185.

Starck, J.-L, Siebenmorgen, R., Gredel, R. 1997, A&A, 482, 1011.

Sui, L., & Holman, G. D.: 2003, ApJ, **596**, L251.

Sui, L., Holman, G. D., & Dennis, B.: 2004, ApJ, 612, 546.

Švestka, Z., Fontenla, J. M., Machado, M. E., Martin, S. F., Neidig, D. F., & Poletto, G. 1987, Sol. Phys., 108, 237.

Thompson, B. J., Cliver, E. W., Nitta, N., Delannée, C., Delaboudiniére, J. P., 2000, Geophys. Res. Lett., 27, 1431.

Wang, H., Qiu, J., Jing, J., & Zhang, H.: 2003, ApJ, **593**, 564.

Webb, D. F., Burkepile, J., Forbes, T. G., & Riley, P., 2003, J. Geophys. Res., 108 (A12), 1440.

Yokoyama, T., Akita, K., Morimoto, T., Inoue, K., & Newmark, J. 2001, ApJ, **546**, L69.
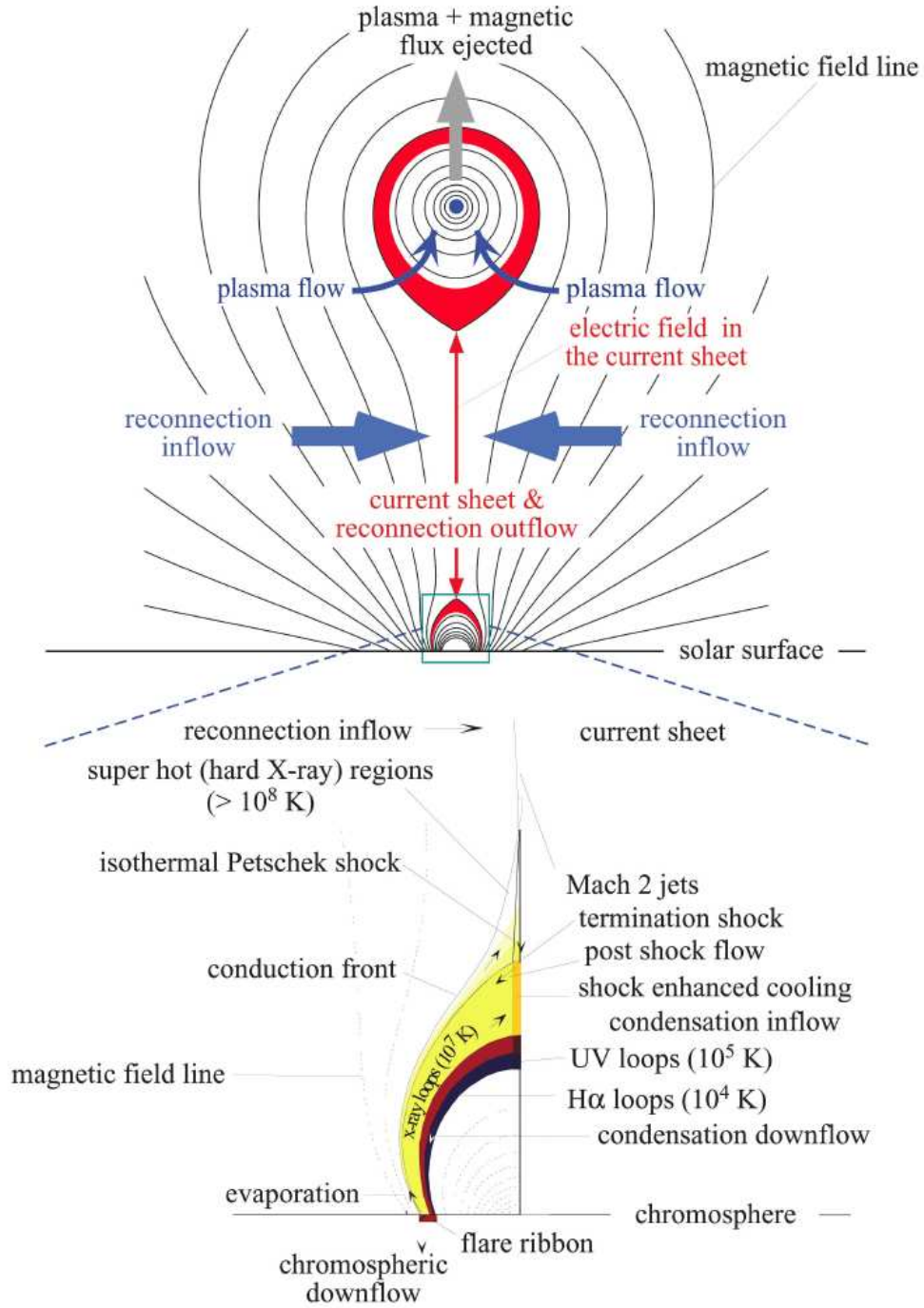

Fig. 1.— Schematic diagram of a disrupted magnetic field that forms in an eruptive process. Colors are used to roughly denote the plasma layers in different temperatures. This diagram incorporates the two-ribbon flare configuration of Forbes & Acton (1996) and the CME configuration of Lin & Forbes (2000). More discussions about the CME part can be found in Lin et al. (2004).
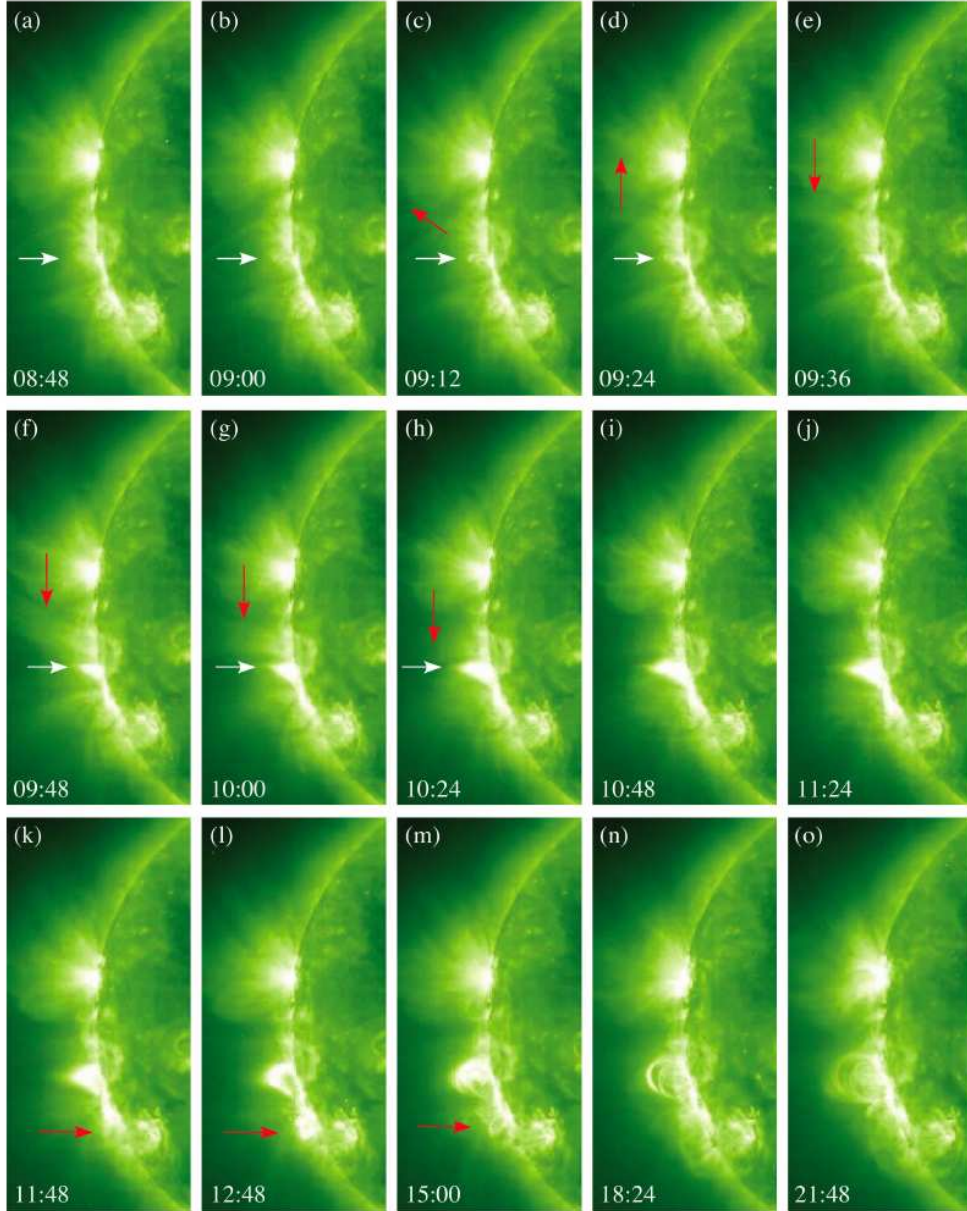
Fig. 2.— EIT 195 Å image set that displays the process that is characterized by the magnetic arcades disruption, the driven magnetic reconnection, and the formation of flare loop system with a cusp structure on the top. The white arrows in panels (a) through (d) indicate the disrupting arcades, the red arrows in (c) and (d) point the direction of the arcade expansion and the arcade leg separation, respectively. The red arrows in panels (e) through (h) show the inflow of magnetic reconnection, and the white arrows in panels (f) through (h) indicate the cusp structure that forms right below the reconnection region. The field of view of each panel is 0.27 $R_\odot$ $\times$ 0.59 $R_\odot$, and all the times are in UT.
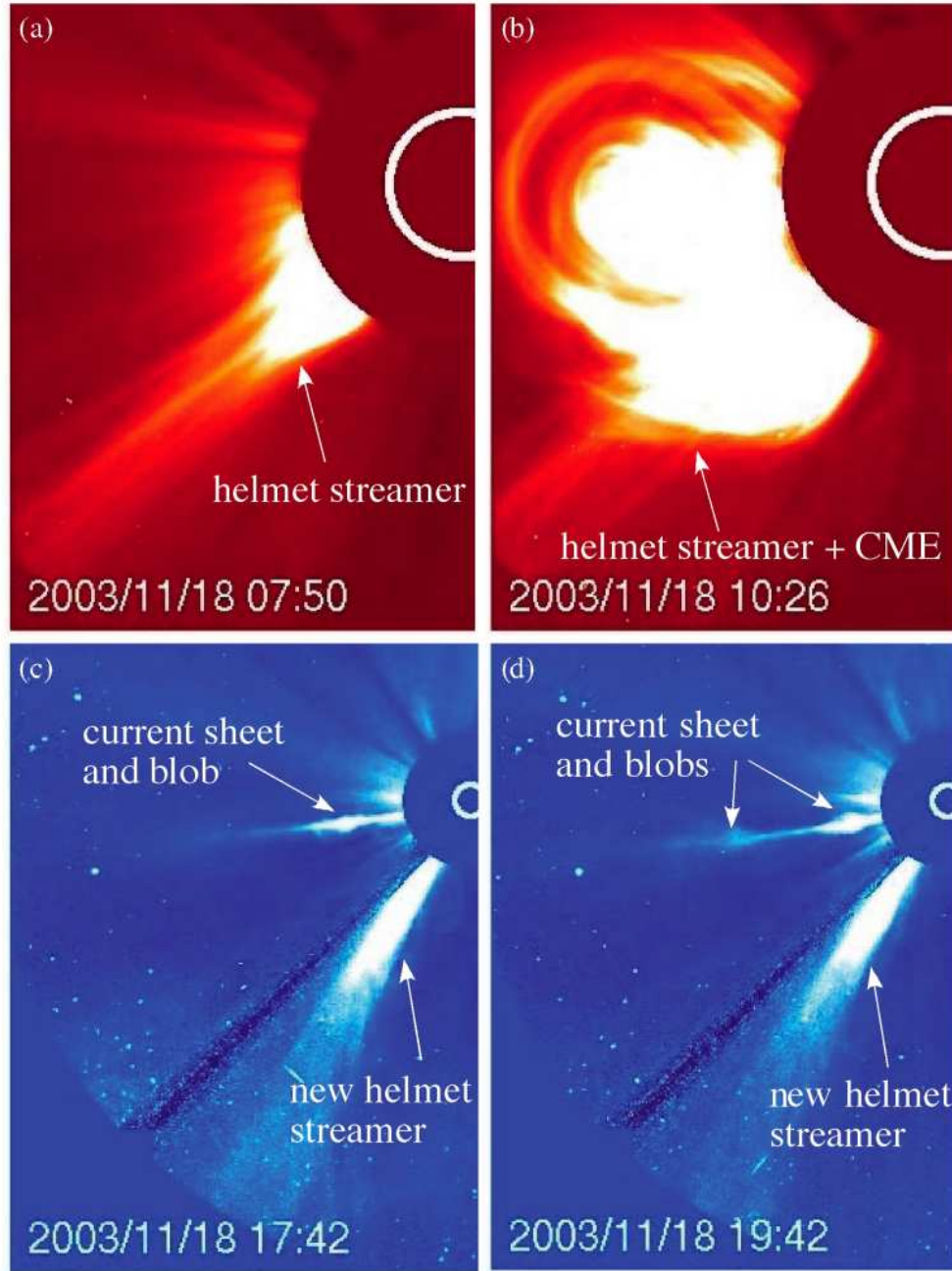
Fig. 3.— LASCO C2 and C3 images. A helmet streamer exists in the region where the CME will go through (a). With rapid expansion of the CME, the helmet streamer is severely deflected from outside (b), and the southern leg of the CME (disrupting arcade) merges with the helmet streamer, forming a new helmet streamer (c and d). A couple of blobs of the reconnected plasma flowing along the current sheet can also be recognized in (c) and (d). All the times are in UT.
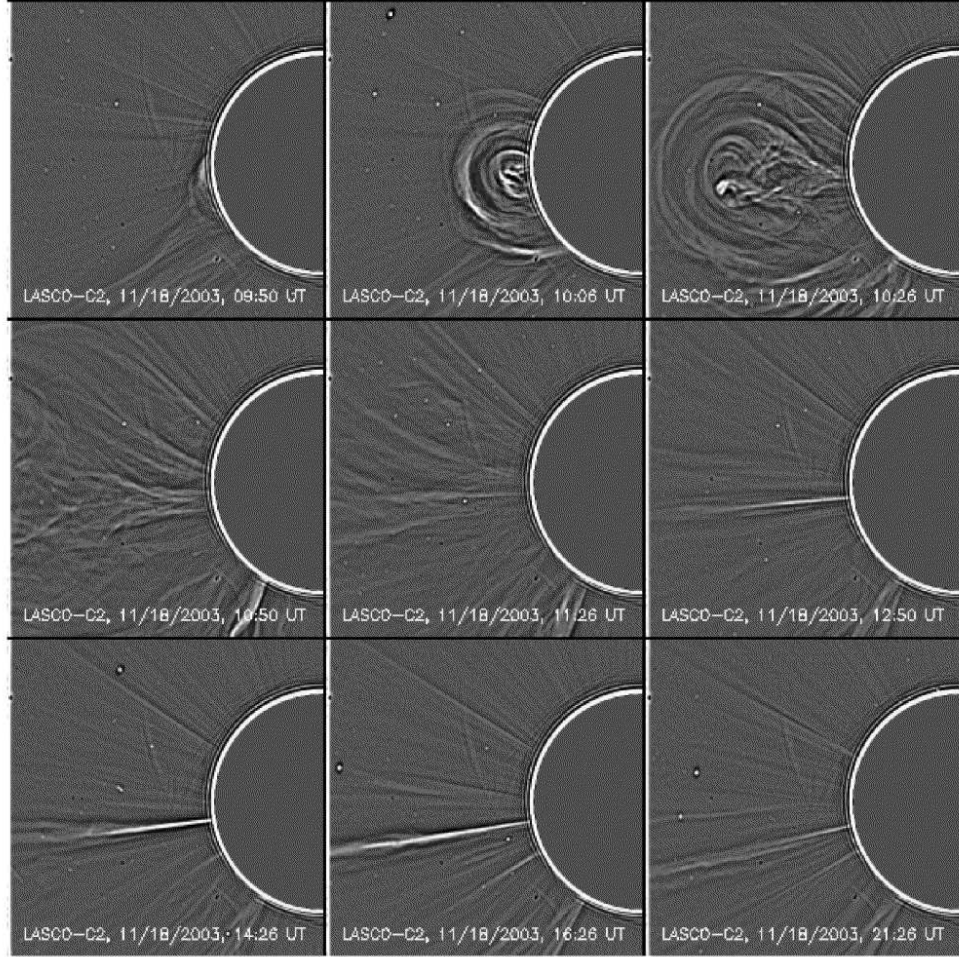
Fig. 4.— LASCO C2 images that have been enhanced by the wavelet technique, which is good at enhancing the fine features of the large scale structures. The leading edge, cavity and core of the CME, as well as the current sheet, are recognized easily.
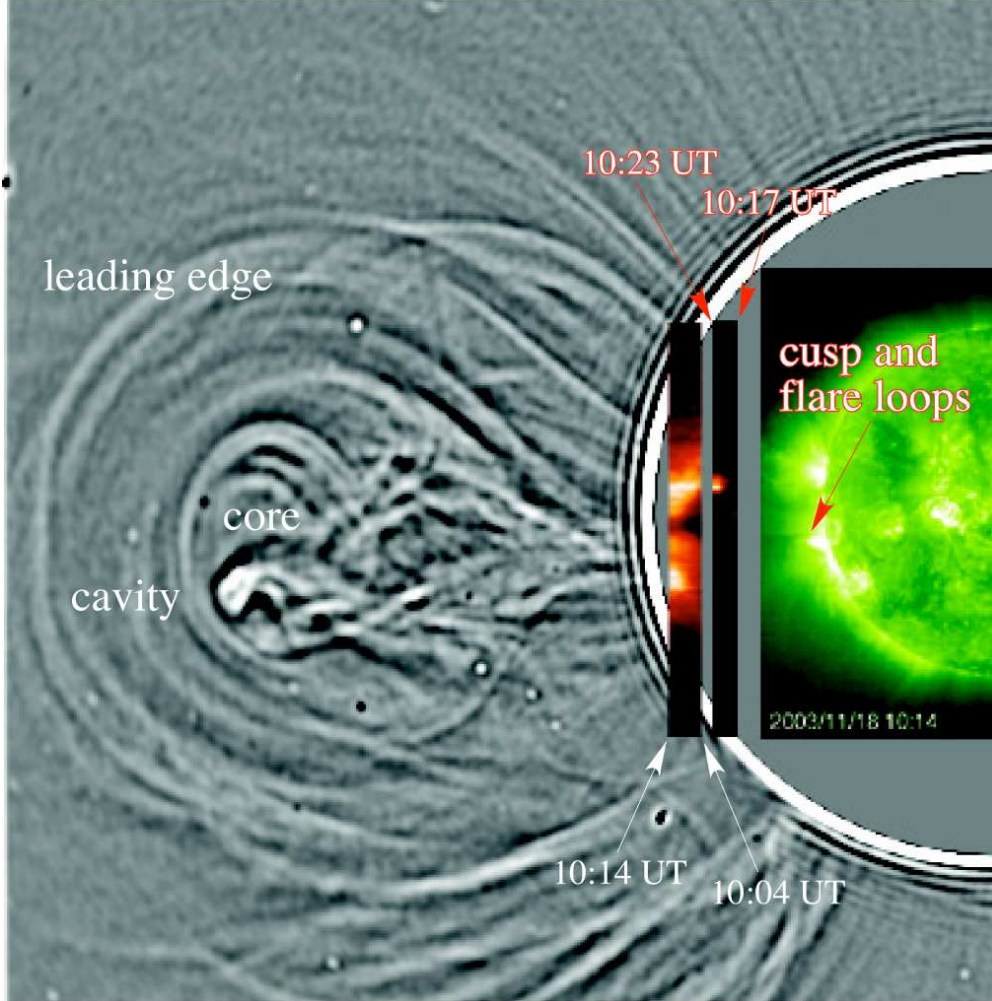
Fig. 5.— C2/UVCS/EIT composite image. The C2 image was taken at 10:26 UT and has been enhanced by the wavelet technique in order to emphasize the morphological features at various positions of the CME, the EIT 195 Å image was taken at 10:14 UT, the left UVCS image is made by stacking 5 UVCS exposures in Lyα that were taken at the altitude of 1.70 R$_\odot$ and covered the time interval from (the right edge) 10:04 UT to (the left edge) 10:14 UT, and the right UVCS image is made by stacking 4 UVCS exposures in Lyα that were taken at the altitude of 1.52 R$_\odot$ and covered the time interval from (the right edge) 10:17 UT to (the left edge) 10:23 UT.
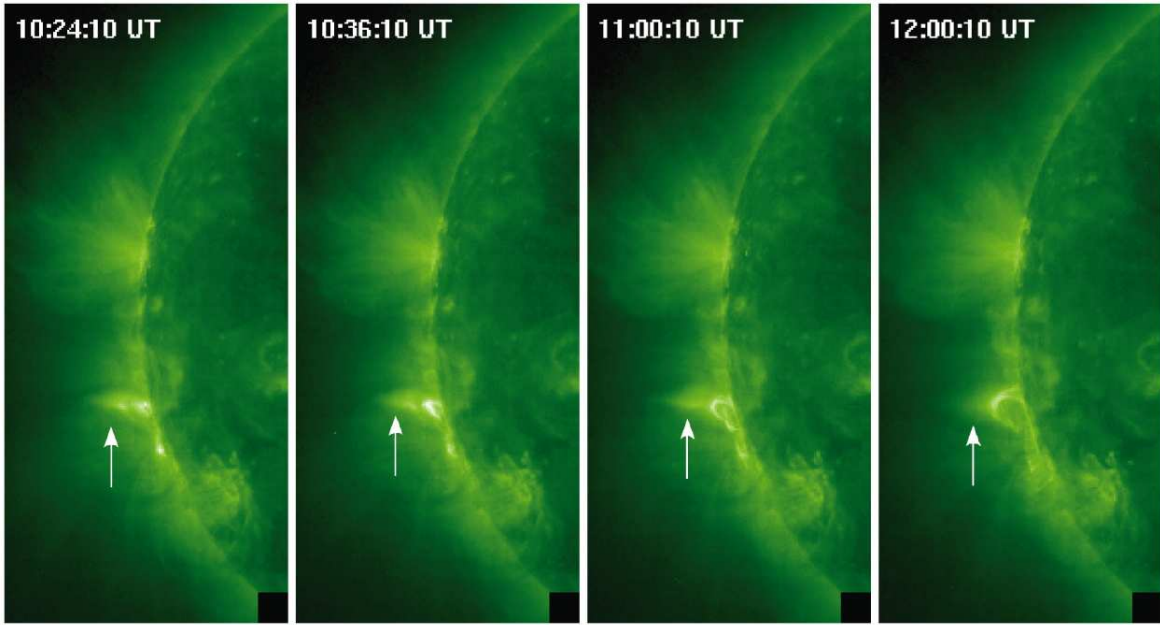
Fig. 6.— Images in EIT 195 Å that have been processed by the WICE technique. Comparing with the corresponding ones in Figure 2, these images show more details of the fine structures between the cusp point and the flare loops. The field of view of each panel is 0.27 $R_\odot$ × 0.59 $R_\odot$.
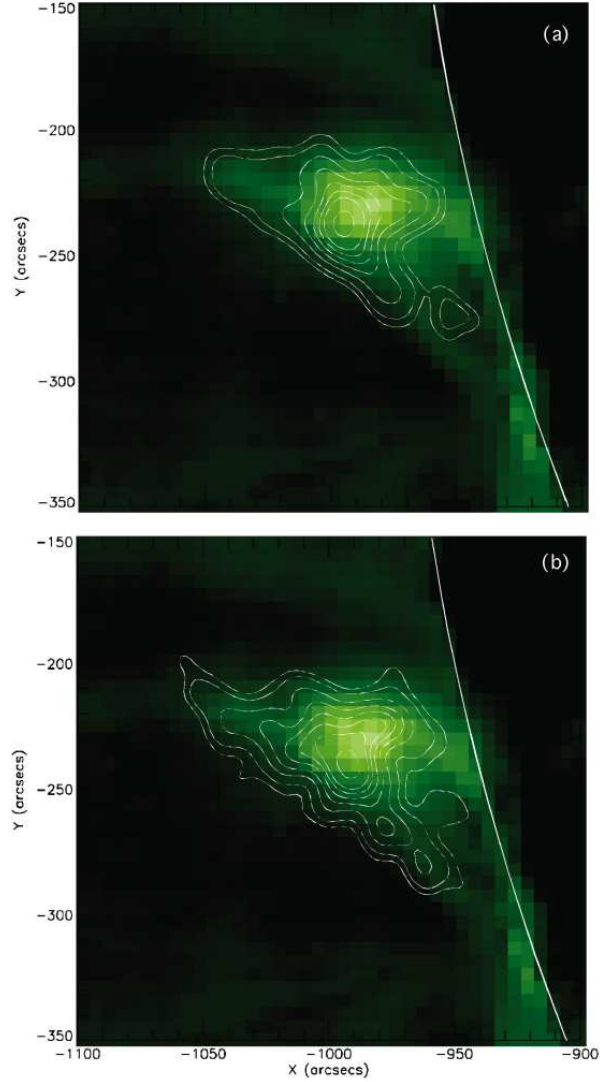
Fig. 7.— Two RHESSI 12-16 keV images (contours) showing the cusp feature over the flare loop system are overlaid on a nearest EIT 195 Å image. RHESSI contours in panel (a) were taken at 09:59 UT and those in panel (b) were taken at 10:02 UT. The contour levels in each image are 15, 20, 30, 40, 50, 60, 70, 80, and 90% of the peak intensity, respectively. The EIT 195 Å images in both panels were taken at 10:00 UT.
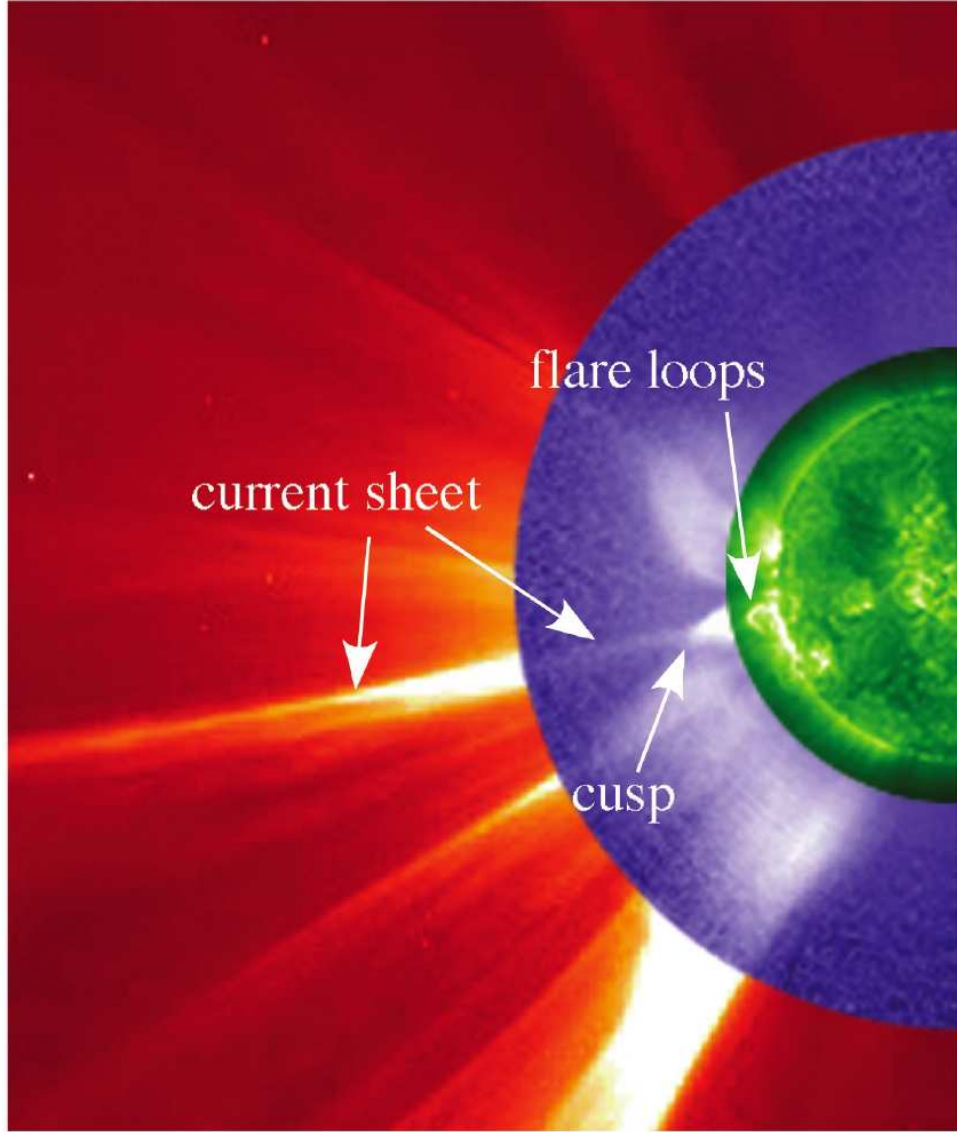
Fig. 8.— Composite of C2 (at 17:50 UT), MK4 (at 17:49 UT) and EIT 195 Å (at 17:48 UT) images. The cusp structure is clearly seen in MK4 white-light image at the lower tip of the current sheet, and a group of flare loops seen in EIT 195 Å image are located right below the cusp point. At this time, the CME has left the field of view for a while. The field of view of MK4 image is 2.76 $R_\odot$ × 5.45 $R_\odot$.
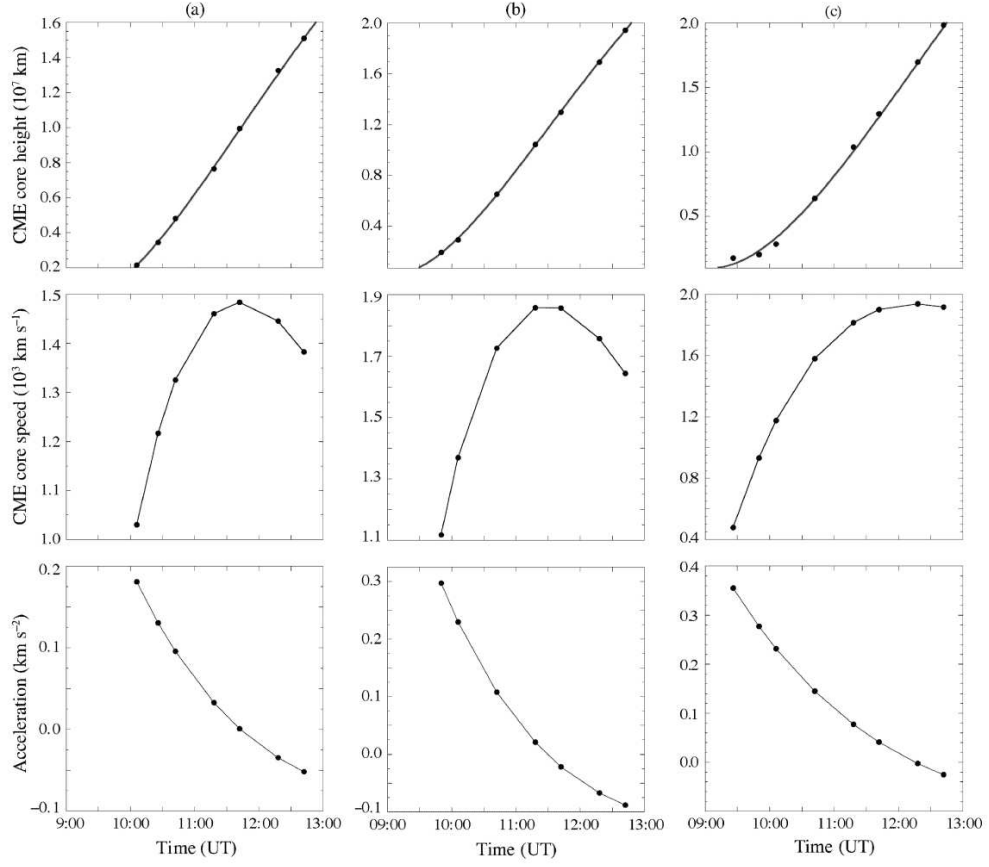
Fig. 9.— Variations of heights, velocities and accelerations of various points on the CME bubble: (a) the CME core at PA = 96°, (b) the CME leading edge at PA = 88°, and (c) the leading edge at PA = 100°.
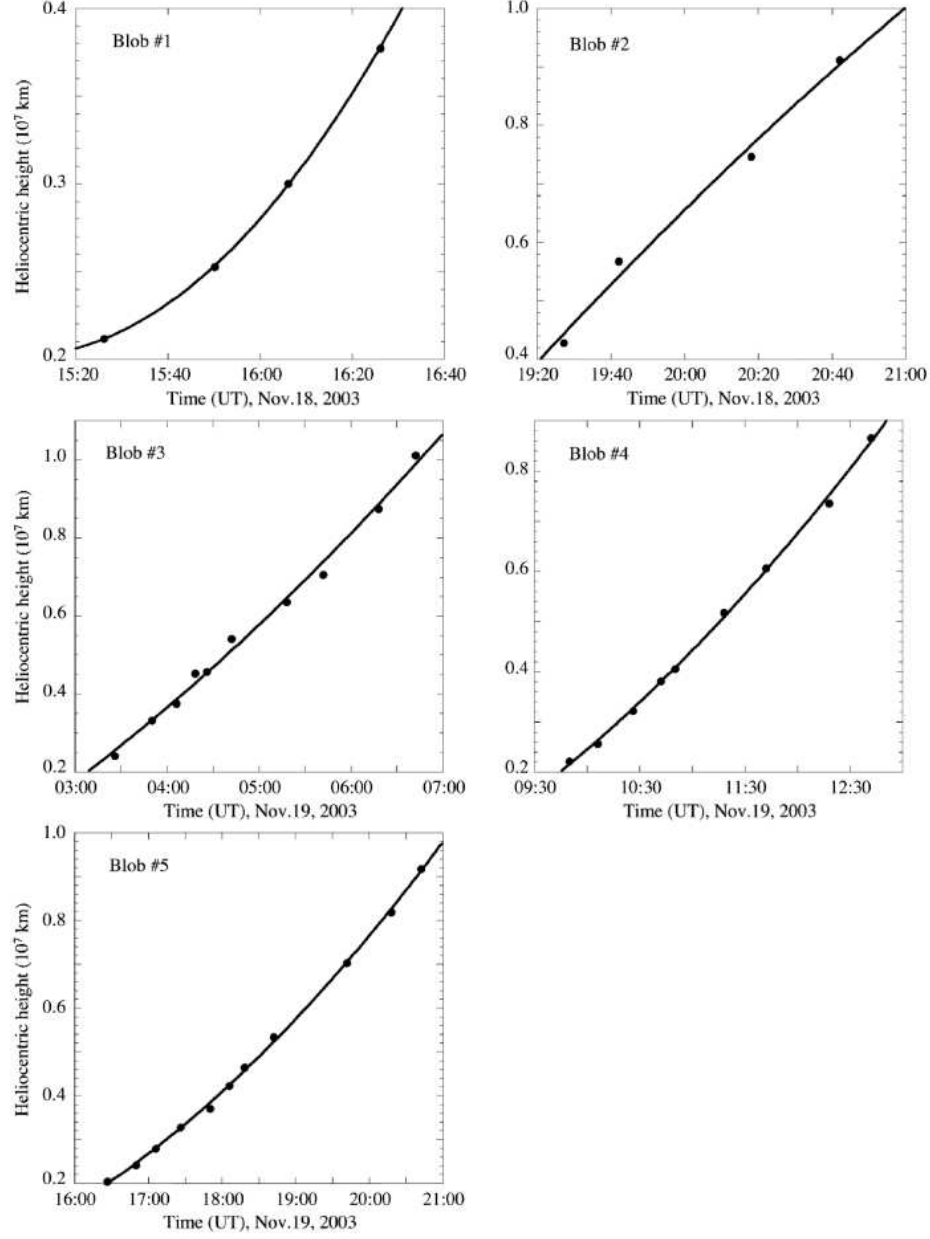
Fig. 10.— Plots of heights versus times for five blobs. The solid circles are observational data and the curves are drawn according to equation (2) with the coefficients given in Table 2.
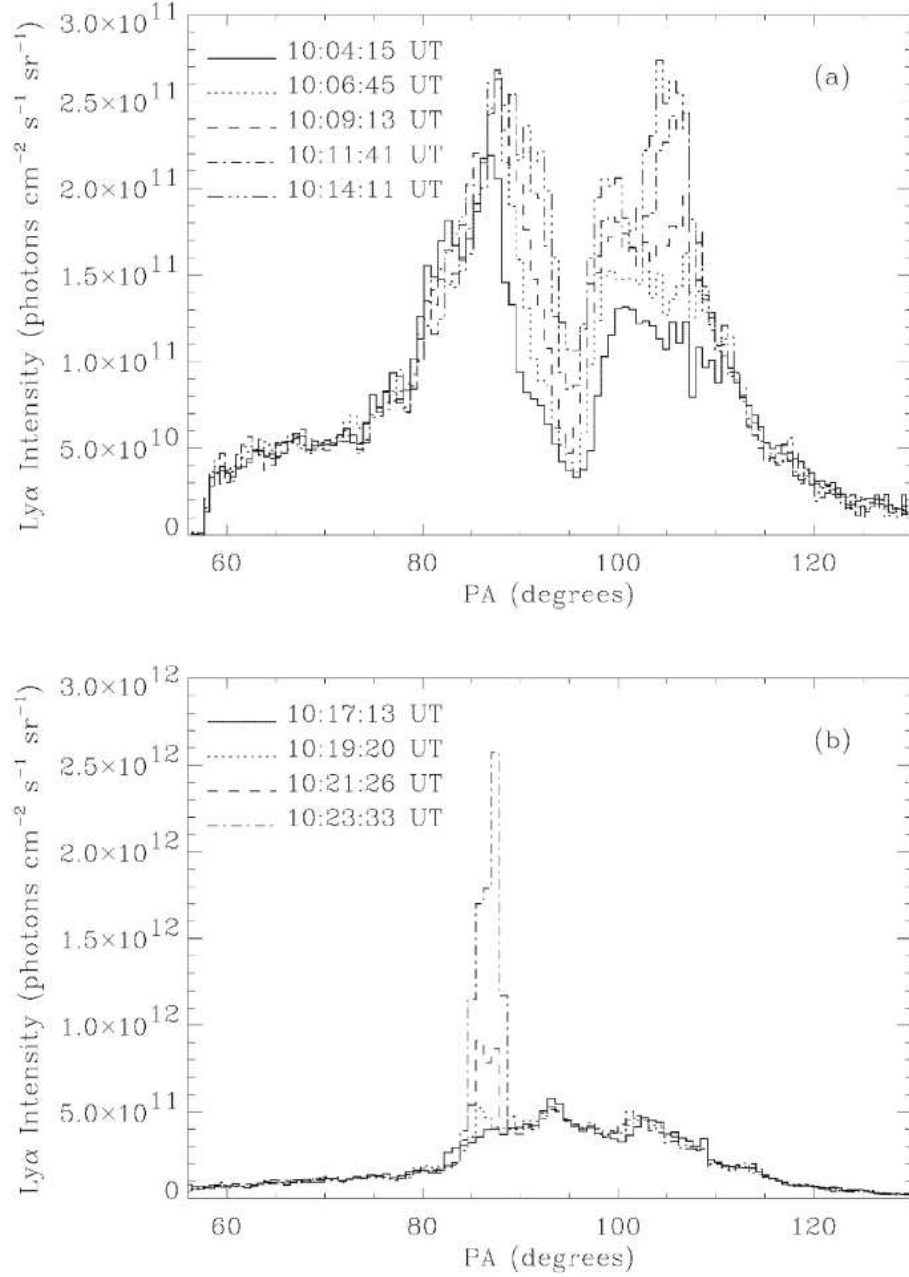
Fig. 11.— (a) Five intensity profiles of Lyα along the UVCS slit taken at 1.70 R⊙ from 10:04 UT to 10:14 UT. The dip on each profile is suggestive of the dark gap shown in Figure 5. Decrease in the depth of the dip or the gap size results from the inflow of the driven magnetic reconnection caused by the eruption at the early stage. (b) Four intensity profiles of Lyα along the UVCS slit taken at 1.52 R⊙ from 10:17 UT to 10:23 UT. A bright feature appears at PA = 88°, and it brightens rapidly.
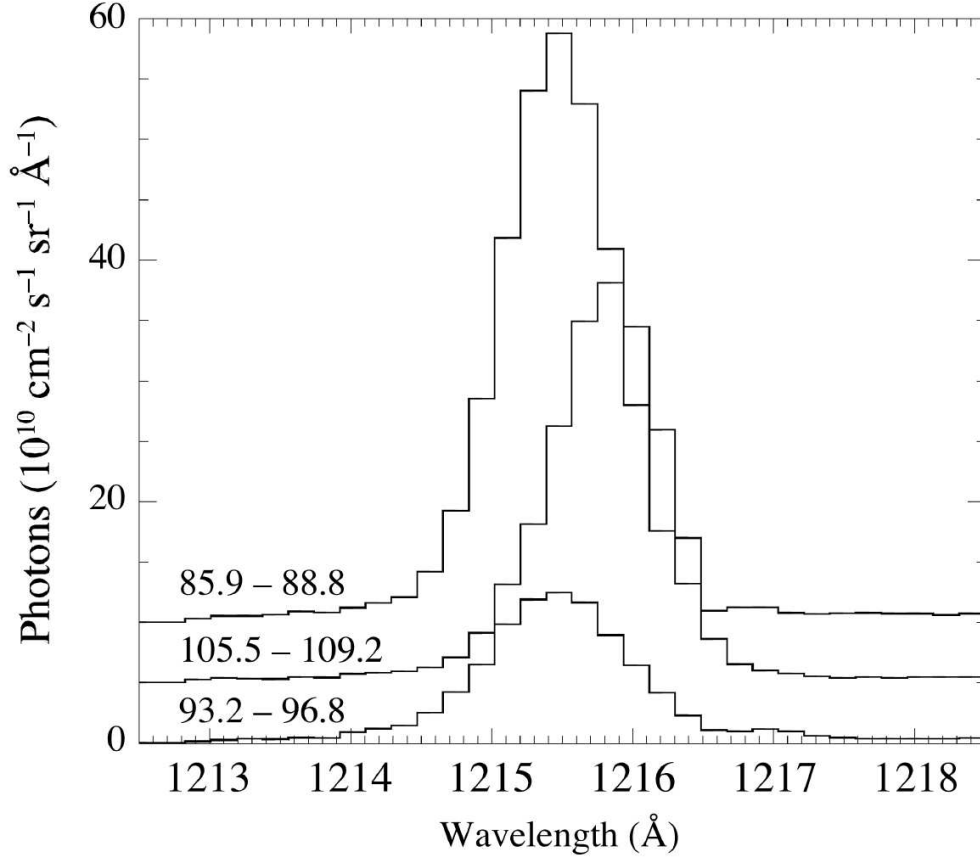
Fig. 12.— Three Lyα intensities as functions of wavelength averaged over different PA ranges that are indicated by each pair of numbers on the corresponding profile: The curve labeled with "93.2 − 96.8" is of the gap, that labeled with "85.9 − 88.8" is of the region north to the gap, and that with "105.5 − 109.2" is of the region to the south. These Lyα profiles are taken at 1.70 R$_\odot$ and also averaged over the time interval from 10:04 UT to 10:14 UT.

Table 1: Coefficients a_i for equation (1) and other parameters.

Objects	a_1 ($\times 10^5$)	a_2 ($\times 10^2$)	a_3	a_4 ($\times 10^{-5}$)	v_{max} (km s^{-1})	t_{max} (UT)	h_{max} (10^6 km)
C. C.[a]	0.41	-1.13	0.21	4.00	1484	11:43	9.95
L. E. 1[b]	2.23	-1.69	0.29	6.55	1865	11:29	11.57
L. E. 2[c]	9.90	-1.53	0.23	5.00	1939	12:15	16.54

[a]CME core at PA = 96°

[b]Leading edge at PA = 88°

[c]Leading edge at PA = 100°

Table 2: Coefficients b_i for equation (2).

Blob	b_1	b_2	b_3	Acceleration (m s^{-2})	Average Speed (km s^{-1})
1	4.05×10^7	-3.49×10^3	7.91×10^{-2}	158	460
2	-6.82×10^7	2.74×10^3	-2.15×10^{-2}	-42.5	1075
3	-2.66×10^6	3.17×10^2	8.39×10^{-3}	16.7	655
4	8.10×10^5	4.05×10^2	1.34×10^{-2}	26.7	573
5	1.49×10^5	2.93×10^2	9.23×10^{-3}	18.5	465